



Moving Ions Vary Electronic Conductivity in Lead Bromide Perovskite Single Crystals through Dynamic Doping

Marise García Batlle, Oriane Baussens, Smaïl Amari, Julien Zaccaro, Eric Gros d'Aillon, Jean-Marie Verilhac, Antonio Guerrero, Germa Garcia-Belmonte

► To cite this version:

Marise García Batlle, Oriane Baussens, Smaïl Amari, Julien Zaccaro, Eric Gros d'Aillon, et al.. Moving Ions Vary Electronic Conductivity in Lead Bromide Perovskite Single Crystals through Dynamic Doping. *Advanced Electronic Materials*, 2020, 6 (10), pp.2000485. 10.1002/aelm.202000485 . hal-02945543

HAL Id: hal-02945543

<https://hal.science/hal-02945543>

Submitted on 22 Sep 2020

HAL is a multi-disciplinary open access archive for the deposit and dissemination of scientific research documents, whether they are published or not. The documents may come from teaching and research institutions in France or abroad, or from public or private research centers.

L'archive ouverte pluridisciplinaire **HAL**, est destinée au dépôt et à la diffusion de documents scientifiques de niveau recherche, publiés ou non, émanant des établissements d'enseignement et de recherche français ou étrangers, des laboratoires publics ou privés.

Moving Ions Vary Electronic Conductivity in Lead Bromide Perovskite Single Crystals through Dynamic Doping

Marisé García-Batlle, Oriane Baussens, Smail Amari, Julien Zaccaro, Eric Gros-Daillon, Jean-Marie Verilhac, Antonio Guerrero, and Germà Garcia-Belmonte*

Metal halide perovskite single crystals are being explored as functional materials for a variety of optoelectronic applications. Among others, solar cells, field-effect transistors, and X- and γ -ray detectors have shown improved performance and stability. However, a general uncertainty exists about the relevant mechanisms governing the electronic operation. This is caused by the presence of mobile ions and how these defect species alter the internal electrical field, interact with the contact materials, or modulate electronic properties. Here, a set of high-quality thick methylammonium lead tribromide single crystals contacted with low-reactivity chromium electrodes are analyzed by impedance spectroscopy. Through examination of the sample resistance evolution with bias and releasing time, it is revealed that an interplay exists between the perovskite electronic conductivity and the defect distribution within the crystal bulk. Ion diffusion after bias removing changes the local doping density then governing the electronic transport. These findings indicate that the coupling between ionic and electronic properties relies upon a dynamic doping effect caused by moving ions that act as mobile dopants. In addition to electronic features, the analysis extracts values for the ion diffusivity in the range of $10^{-8} \text{ cm}^2 \text{ s}^{-1}$ in good agreement with other independent measurements.

1. Introduction

Apart from being used as light-absorbing materials for photovoltaic applications,^[1] hybrid perovskites have recently attracted much attention as sensitive layers for high-energy radiation detectors and imaging devices for medical diagnostics.^[2] In some aspects, X- and γ -ray detection technologies face similar drawbacks when using perovskite materials as those previously encountered in solar cell engineering. One of them is caused by the presence of mobile ions and how these species alter the internal electrical field, interact with the contact materials, or modulate electronic properties.^[3–6] Upon biasing, charged moving ions accumulate in the vicinity of the outer interfaces causing electrical field partial shielding.^[7–9] It has also been reported how intrinsic defects chemically react with the electrodes giving rise to losses in performance and device instabilities.^[10,11]

The occurrence of polarized interfaces in hybrid perovskite-based electronic devices was proposed^[12] as an explaining mechanism for the measured excess capacitance at low frequencies. In dark conditions, mobile ions pile up at outer interfaces forming double layer-like structures in the vicinity of the perovskite/contact interface.^[13,14] Excess dark capacitance of order $1\text{--}10 \mu\text{F cm}^{-2}$ can be readily explained in this way. In addition to purely electrostatic approaches for the interfacial phenomena, it is known that chemical reactions between mobile ions and contacting materials might give rise to the formation of dipole-like structures.^[15,16] Also, deviations from stable electrical characteristics (i.e., hysteresis in current density-voltage $J\text{--}V$ or non-ohmic response) have previously been correlated with the dynamics of migrating ions that interact with the contacts.^[14,15,17] A survey about the chemical reactivity of the perovskite/contact materials can be found elsewhere.^[14] In this sense, the kinetics of electrode charging may be understood not only in terms of ion diffusion and double-layer formation, but also by interface reactivity forming local chemical bonds. Therefore, the variety of interfacial-related mechanisms, from purely electrostatic to chemically active, makes the interpretation of the registered electrical response largely dependent on the specific selected materials and device processing.


M. García-Batlle, Dr. A. Guerrero, Prof. G. Garcia-Belmonte
Institute of Advanced Materials (INAM)

Universitat Jaume I
ES12006, Castello, Spain
E-mail: garciag@uji.es

O. Baussens, Dr. E. Gros-Daillon
Grenoble Alpes University
CEA
LETI

F38000, Grenoble, France
S. Amari, Dr. J.-M. Verilhac
Grenoble Alpes University
CEA
LITEN

F38000, Grenoble, France
Dr. J. Zaccaro
Grenoble Alpes University
CNRS
Grenoble INP
Institut Néel F38042, Grenoble, France

 The ORCID identification number(s) for the author(s) of this article can be found under <https://doi.org/10.1002/aelm.202000485>.

DOI: 10.1002/aelm.202000485

A strategy to progress in relating electric responses, operating mechanisms, and device architecture relies upon simplifying the probing structure mainly in two aspects. One of them, by using single-crystal samples instead of polycrystalline layers that introduce additional uncertainties with respect to the effects of grain boundaries and internal interfaces.^[18–21] The other simplification consists in selecting symmetrical samples with less reactive or passivated contacts, which improves reproducibility and limits outer interface influences on the overall electrical response.^[22] This last point is particularly important when long-time experiments are programmed. Commonly observed drifts and instabilities in the electrical response are not easily connected to well-identified evolving mechanisms, in such a way that the underlying uncertainty about governing processes persists.

Here, high quality methylammonium lead tribromide (MAPbBr₃) single crystals are contacted with chromium electrodes. Thermally evaporated chromium has been selected as a material that spontaneously oxidizes during sample preparation due to a very negative standard reduction potential, giving rise to a thin layer of Cr₂O₃.^[23] The passivation of the interface occurs by Cr(III) formation making the electrode material less reactive than other metals as Au when put into contact with the perovskite layer.^[24] Using Cr as metal contact has proved successful in increasing the stability in record photovoltaic devices due to the deactivation of one of the possible degradation pathways.^[22,24,25] Also for high-sensitivity and long-stability X-ray detectors, chromium-based contacts have been employed.^[26,27]

For the purpose of this work, the use of more stable Cr contacts provides unambiguous access to the electrical dynamics of migrating ions in the bulk of the perovskite and their relaxation kinetics.^[28] It is revealed here that there exists an interplay between the perovskite electronic conductivity and the defect distribution within the crystal bulk. It is shown how the ion dynamics effectively governs the electronic properties by changing the local doping density. These findings clearly indicate that the interplay between ionic and electronic properties in perovskite materials relies upon a sort of dynamic doping effect caused by moving ions that act as mobile dopants. In addition to electronic features, our analysis extracts values for the ion diffusivity in the range of 10^{−8} cm² s^{−1} in good agreement with independent measurements.

2. Results

Single-crystal MAPbBr₃ were prepared following the growth methodology detailed in a previous work.^[29] Single crystals obtained have been characterized by cross-polarized light, surface chemical etching to reveal dislocations, and X-ray diffraction (FWHM with an average of 28.3 arcseconds). By this method, a clear improvement in crystal quality is reached with higher transparency (≈80%), minimized internal strains, and a low dislocation density in the range of 10⁴–10⁵ cm^{−2}.^[29]

We show here the general electrical behavior of single-crystal perovskite samples of MAPbBr₃ with thickness of ≈1 mm, symmetrically contacted with Cr electrodes (for sample details, see Supporting Information and Experimental Section). By examining **Figure 1**, one can infer that the current–voltage: *I*–*V*

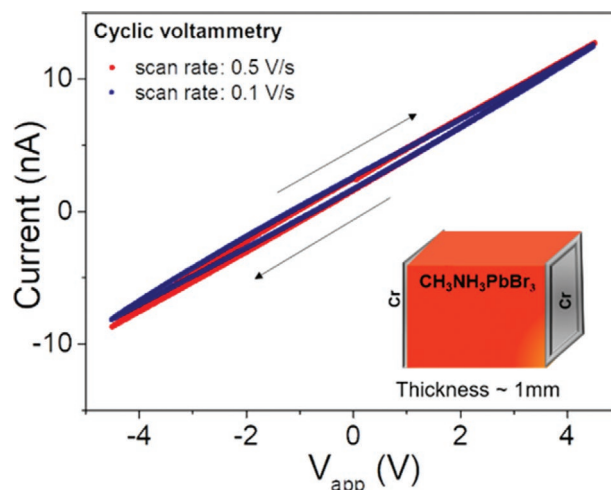


Figure 1. Example of current–voltage characteristics of MAPbBr₃ single crystals of thickness ≈1 mm symmetrically contacted with Cr electrodes. The utilization of two different scan rates allows evidencing a small hysteretic contribution caused by additional capacitive currents. It is noted the time window of minutes for data registering.

characteristics exhibit an approximate ohmic response within the selected voltage range. Accompanying the operation ohmic current, a hysteretic current appears as a consequence of the capacitive mechanisms occurring at low frequencies (see below for impedance analysis).^[10] It is remarkable that the ohmic character of the characteristics is in agreement with previous analysis on Cr-contacted perovskite devices.^[30] On the contrary, Au metal as contact material yields much more featured responses.^[15]

All impedance measurements are performed at room temperature, in the dark, and air ambient conditions. This experimental setup avoids the formation of an internal built-in potential as expected when asymmetrical (different work function) materials are used as selective contacting layers. One can observe in the impedance (**Figure 2a**) and capacitance (**Figure 2b**) responses, registered at zero-bias, two main features: at high and intermediate frequencies ($f > 100$ Hz), the geometrical capacitance C_g and sample resistance R dominate. This forms a semicircle in **Figure 2a** through the parallel combination RC_g . At lower frequencies, the commonly reported excess capacitance increment $C_s \gg C_g$ is observed in **Figure 2b**, which is viewed as additional increment in the impedance plot. The low-frequency feature in the dark has been usually related to ionic polarization/dynamics within the crystal,^[12] and is responsible for the *I*–*V* distortion (hysteresis) in **Figure 1**. The spectra are analyzed and fitted in terms of the equivalent circuit given in **Figure S1**, Supporting Information.

One important question is to verify whether the high-frequency impedance response actually stems from bulk mechanisms. To this end, an exhaustive test has been performed by varying the single-crystal thickness. The diameter of the impedance arc should relate to the electronic conductivity $\sigma_e = qn\mu_e$, which establishes the sample (high-frequency) resistance as $R = L/\sigma_e A$, where q is the elementary charge, n is the carrier density gathering both electrons and holes, μ_e is the electronic carrier mobility, L corresponds of the sample thickness, and A

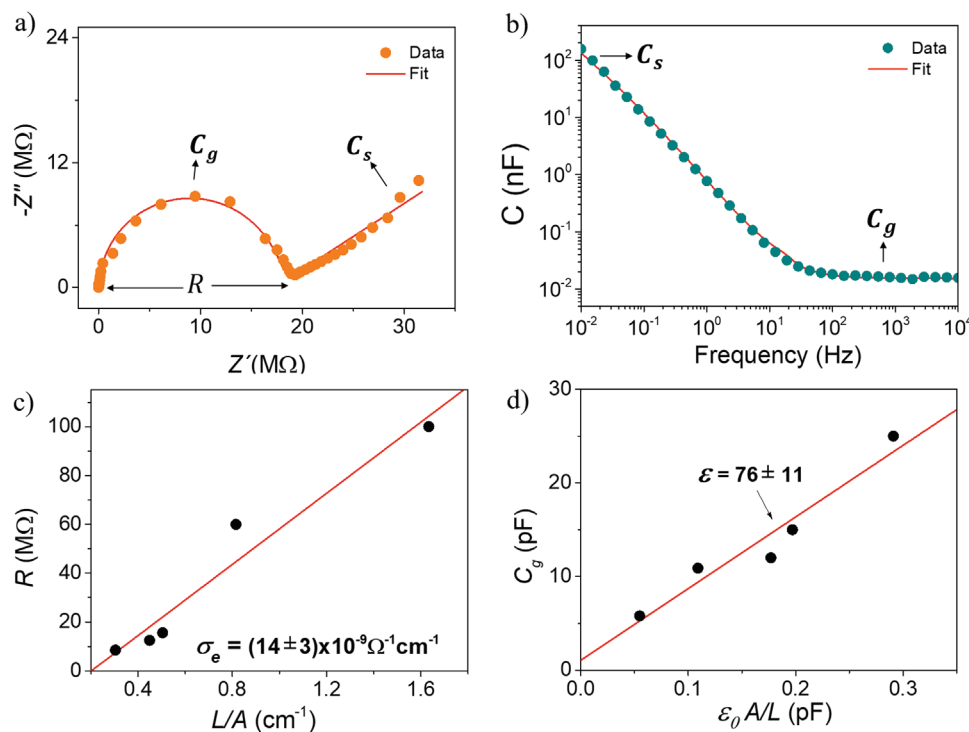


Figure 2. a) Example of the impedance response of MAPbBr₃ single crystals of thickness ≈ 1 mm symmetrically contacted with Cr electrodes measured at 0 V in the dark (relaxed samples). Fits result by using the equivalent circuit of Figure S1, Supporting Information. b) Capacitance spectrum. Scaling of the high-frequency c) resistance and d) capacitance for five samples of different thicknesses and electrode area, exhibiting linear relationship with geometrical parameters.

its effective area. It is assumed that $\sigma_e \gg \sigma_i$ by several orders of magnitude so as to establish the high-frequency resistive response. See below our discussion on the doping character of the samples. Similarly, the capacitive mechanism ought to scale with thickness as $C_g = \epsilon \epsilon_0 A/L$, ϵ being the dielectric constant and ϵ_0 the permittivity of the free space. As observed in Figure S2, Supporting Information, the high-frequency capacitance exhibits no variation upon biasing or time. Therefore, the parallel combination RC_g determines the high-frequency part of the spectra and is completely given by electronic transport and dielectric properties.

By examining Figure 2c,d, one can infer that both R and C_g scale following the predicted dependence on geometric factors. The dielectric constant $\epsilon = 76 \pm 11$ extracted from linear fitting agrees with previous determinations for MAPbBr₃,^[31–33] which resulted in values $\epsilon \approx 60$ at 300 K. Also, the crystal electronic conductivity can be inferred from the linear relationship $R \propto L/A$. Here, electronic conductivity of the measured single crystals is in the order of $10^{-8} \Omega^{-1} \text{cm}^{-1}$. High electronic mobility has been measured using laser time-of-flight techniques in our samples $\mu_e = 13 \text{ cm}^2 \text{V}^{-1} \text{s}^{-1}$,^[34] in accordance with previous analysis on perovskite single crystals.^[35] These mobility values allow us to infer a background carrier density $n = 1.3 \times 10^{10} \text{ cm}^{-3}$, that also agreed with previous estimations.^[20] As both parameters linearly scale with the geometrical values, we conclude that the high-frequency part of the impedance response obeys electronic bulk conductive and dielectric properties of MAPbBr₃ single crystals.

Having established the bulk origin for the experimental R and C_g values, we explore now the effects upon bias application. By examining Figure 3a, one can observe that biasing between 0 and 5 V increases the main resistance (high-frequency part), which is related to the conduction properties of the perovskite crystal as discussed previously. In these experiments, impedance measurement was performed at a given applied voltage after 5 min of pre-conditioning time in the dark. Therefore, the total poling time at each bias is estimated to be of 20 min. It is noted that the linear low-frequency feature is less visible for >2 V bias. After removing applied voltage, the samples are able to recover initial (equilibrium) response at 0 V bias, although it takes a much longer time (≈ 24 h) as illustrated in Figure 3b. A detailed view of the decreasing high-frequency resistance for the last 5 h after removing 5 V bias is shown in Figure 3c. It is noted that in addition to a well-defined semicircle, a line at low frequencies points to the occurrence of modulated resistive/capacitive contributions only observable at longer times.

One can infer from our observations that sample resistance is a function, not only of the applied bias, but also of the poling and recovering time. While poling induces relatively quick responses with resistive increment as main result, equilibrium state needs much longer times to recover. The above explained impedance variation process was repeated several times to verify its cyclability (see reproducibility test in Figure S3, Supporting Information). It is important to note that due to the use of Cr, we are able to limit the interference of the contacts by

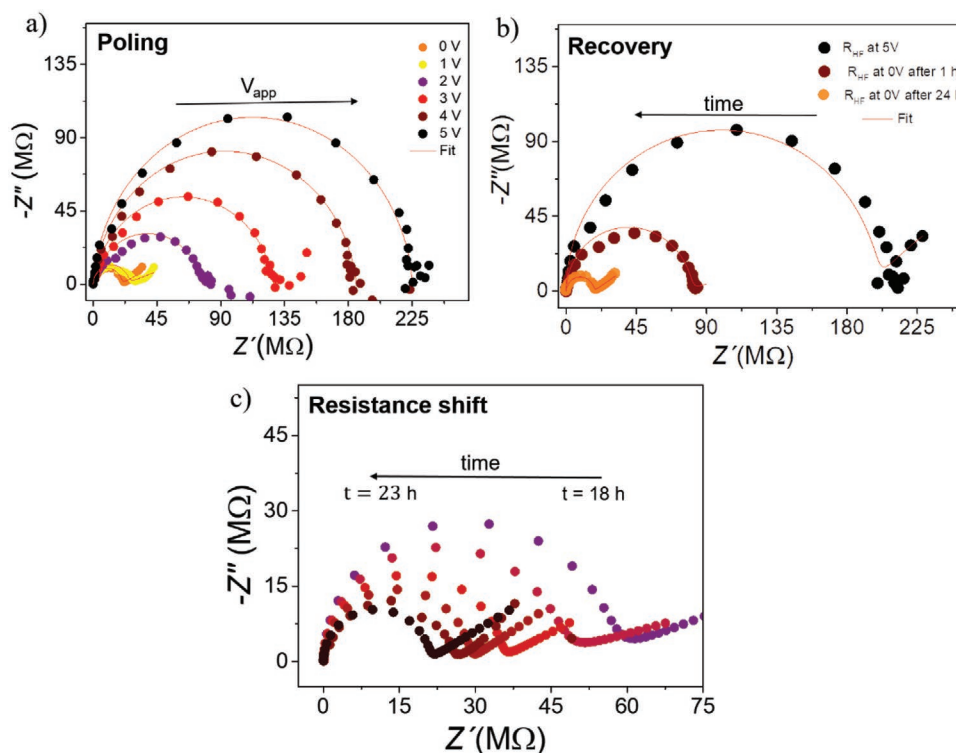


Figure 3. a) Variation of the impedance as a function of the increasing bias with total measuring time ≈ 20 min at each voltage. b) Variation of the impedance after removing 5 V bias and evolution with time. Note that the final (24 h) spectrum recovers the initial one at 0 V bias in (a). c) Detailed view of the variation of the impedance after removing 5 V bias and evolution with time for smaller impedances (five last hours of the experiment).

chemical reactivity. Therefore, these findings suggest a plausible change in electrical driving force ultimately establishing the conductive character of the bromide perovskite crystals.

A complete series of impedance spectra allows calculating how the value of the high-frequency resistance recovers the equilibrium after bias is removed (see Figure 4). It is inferred that the resistance shows a large value R_1 at shorter recovering times and progressively attains a steady-state value R_0 after a

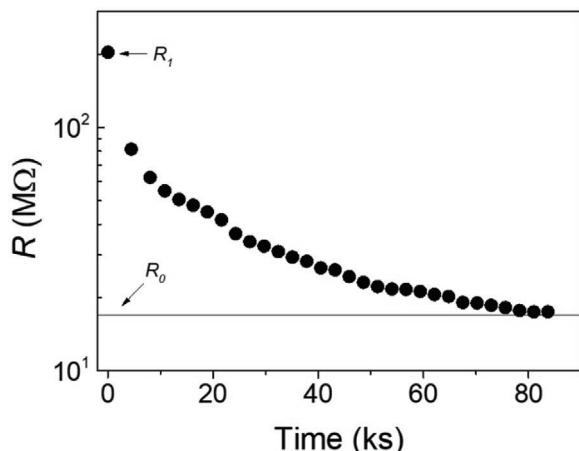


Figure 4. Variation of the resistance extracted from fitting of impedance spectra after bias removing at $t = 0$. Note the log scale in the vertical axis that informs on the complex function (non-exponential) of the resistance variation.

long equilibration time of ≈ 24 h. It is also seen that the resistance variation does not obey an exponential law.

In order to understand this variation, we propose a rationale that connects the decrease of the resistance with time with the increase in electronic doping of the perovskite bulk. Our hypothesis is that the carrier density n depends on the distribution of mobile ions within the crystal that acts as moving dopants. This kind of correlation between mobile ion location within the crystal and electronic carrier density was previously postulated by Bisquert and co-workers in the case of the electrical switching of photoluminescence.^[36]

Upon long-time polarization, ion movement and accumulation produce a sort of de-doping effect giving rise to a reduced carrier density n_1 in a wide portion of the crystal, and consequently yields larger resistance R_1 . After removing bias, ions take some time to return to their initial distribution that recovers the greater background value of the carrier density n_0 along the crystal bulk. That initial carrier density is understood as an equilibrium value for the sample at zero bias in the dark. From the evolution of the impedance with time, it is observed that $R_0 < R_1$, or equivalently $n_0 > n_1$. From the values in Figure 4, one can infer that electronic carrier density ratio n_0/n_1 attains values as high as ≈ 12 , thus indicating that doping is reduced by approximately one order of magnitude upon 5 V poling. The time evolution of the ionic-electronic coupling is schematically illustrated in Figure 5 through the dynamic doping process.

Let us consider that the rate at which n transits from n_1 to n_0 mimics the time scale of mobile ion redistribution after releasing. For the sake of simplicity, we model the increase in

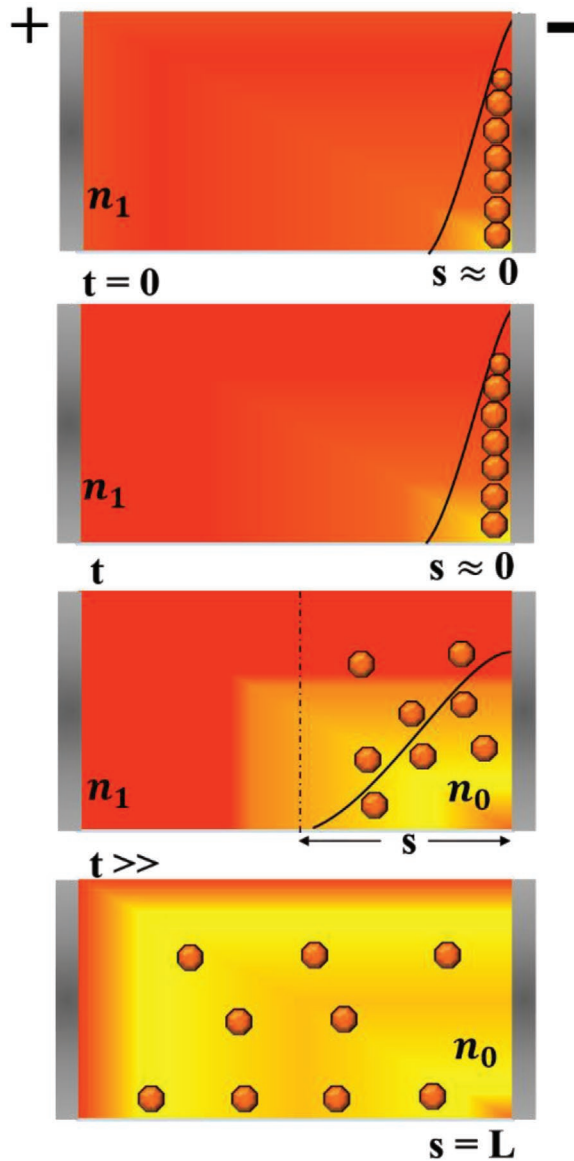


Figure 5. Schematic drawing of the ion polarization and rearrangement process (dynamic doping) by diffusion after bias removing. Initially, mobile ionic species accumulate following a narrow distribution near the contact. Here, it is assumed that positively charged defects dominate the concentration of mobile ions. Ion accumulation entails de-doping of electronic carriers within the crystal bulk with carrier density n_1 . At $t = 0$, external electrical field is removed so that ions are released and start diffusing. At a given releasing time t , the ion distribution width s spreads and provokes a progressive increment in the overall carrier density n . In the final stage, ions recover the equilibrium distribution and, consequently, the overall electronic carrier density returns to n_0 .

average carrier density in relation to the effective size s occupied by moving ions. At shorter times, ion accumulation restricts to narrow layers in the vicinity of the contact (see Figure 5). Ideally, s evolves after bias removing from $s \approx 0$ to L . As a first approximation, one can assume that the effective size s divides the bulk into two zones of larger and smaller doping, forming a sort of semiconductor homojunction in which the boundary position varies with time. The real situation is of course much

more complex and should include the exact distribution of mobile ions and their contribution to local electronic doping.

For the sake of simplicity, an effective carrier density can be calculated as

$$n = \frac{1}{L} [n_0 s + n_1 (L - s)] \quad (1)$$

which includes two zones of different doping. It should be noted that two well-differentiated impedance arcs corresponding to each of the above-mentioned separate doping zones are hardly observable because of the rather small ratio $n_0/n_1 \approx 12$. After rearrangement, Equation (1) can be expressed as

$$n = n_1 \left(1 + \frac{\gamma s}{L} \right) \quad (2)$$

here, γ represents a constant determined by the limiting doping states

$$\gamma = \frac{n_0 - n_1}{n_1} \quad (3)$$

that results by assuming $n(s=0) = n_1$ and $n(s=L) = n_0$.

Let us also assume that doping ions initially accumulate following a narrow distribution near the contact that spreads as $s = \sigma$. Here, σ stands for the distribution width. The accumulation occurs by effect of the applied electrical field because no built-in potential exists for symmetrically contacted samples. This ionic accumulation is expected by formation of a diffusion ion layer in the vicinity of the contacts and by very limited interfacial chemical interaction within the experimental time framework. When bias is removed, ions are released and tend to diffuse back to their equilibrium position in such a way that the mean square displacement of the ion distribution enlarges with time. The simple outlined model would entail diffusion takes place in 1D ($\delta = 1$), but the real situation should be more complex with diffusion dimensionality approaching larger values. Individual ion penetration path is in principle hemispherical. Therefore, the distribution width spreads by diffusion as

$$\sigma = \sqrt{2\delta Dt} \quad (4)$$

where D accounts for the ion diffusion coefficient, $\delta = 3$ for 3D diffusion, and t is the time.

Because the resistance ratio R_1/R equals the density ratio n/n_1 , one can derive by combining Equations (2) and (4), and $\delta = 3$ an expression for the time dependence of the resistance ratio as

$$\frac{R_1}{R} = 1 + \frac{\gamma}{L} \sqrt{6Dt} \quad (5)$$

which predicts a linear dependence as $\propto \sqrt{t}$ with slope determined by the diffusion coefficient.

The resistance extracted from impedance data fitting in Figure 4 is replotted in Figure 6 in accordance to the formulation of Equation (5), i.e., R_1/R as a function of \sqrt{t} .

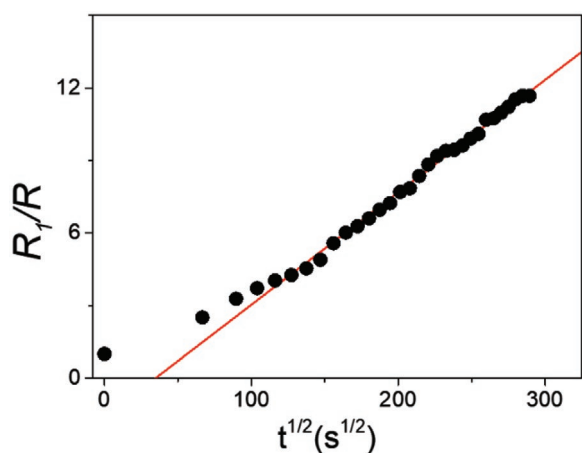


Figure 6. Variation of resistance ratio as a function of time following the relationship of Equation (5). Solid line represents a linear fitting.

As observed, a good linear relationship is reproduced between R_1/R and \sqrt{t} in accordance with our prediction for longer times. A deviation occurs at shorter times, presumably related to the simplicity of the model in Equation (5), unable to capture second-order depolarization effects for greater moving ion concentrations. It is also questionable that our assumption $s = \sigma$ is valid for $s \ll L$. In any case, from the linear fitting slope in Figure 6 (valid for longer times) and the experimental parameters $L = 0.88$ mm and $\gamma = 10.67$, one can obtain a value for the ion diffusion coefficient that results in $D = 2.6 \times 10^{-8}$ cm² s⁻¹. We note that reducing the diffusion dimensionality from $\delta = 3$ to $\delta = 1$ just enlarges the diffusion coefficient by a factor three. Whereas some studies have reported diffusivity values of native defects in organohalide perovskites of the order of those encountered in common solid-state ionic conductors, $D \approx 10^{-12}$ cm² s⁻¹,^[37–39] other analysis gave much faster ion migration coefficients $D \approx 10^{-8}$ – 10^{-7} cm² s⁻¹ in agreement with recent determinations and simulations of the diffusion coefficient.^[40,41]

3. Discussion

We remark that ionic diffusion coefficients in the order of 10^{-8} – 10^{-7} cm² s⁻¹ explain the extremely slow relaxing time (≈ 24 h) after bias removing in the studied perovskite thick single crystals. Similarly, it is also possible to estimate the short polarization time upon poling evidenced in Figure 3a. Resistance attains large values a few minutes after bias application. From the estimated D and using the Einstein relation $\mu_i = qD/k_B T$, μ_i being the ionic mobility and $k_B T$ the thermal energy, one can estimate the ion transit time by electrical field drift upon application of 5 V bias as $t_d = L^2/\mu_i V_{app}$. For our measurements, the transit time calculation results in polarization times of $t_d \approx 15$ min, which agrees with our general observation about the impedance dynamic change in Figure 3a. Therefore, it is concluded that polarization by ion movement (drift-driven) takes several minutes for 1 mm-thick single crystals, but requires much longer times when ions should be transported by diffusion. As observed by impedance measurement, ion distribution locally

varies the electronic doping and the overall sample resistance. More importantly, it is the ion dynamics that governs the ultimate response time of the electronic transport in perovskite compounds through the dynamic doping process.

Also of importance is the comparison between electronic and ionic mobilities. As noted, electronic conductivity situations in values as high as $\mu_e = 13$ cm² V⁻¹ s⁻¹ for high-quality single crystals. From our estimations, the ionic mobility results in $\mu_i = 1.0 \times 10^{-6}$ cm² V⁻¹ s⁻¹, and therefore $\mu_e \gg \mu_i$ as expected. In order to achieve similar ionic and electronic conductivities $\sigma_e \approx \sigma_i$, mobile ion concentration as high as 1.7×10^{17} cm⁻³ would be necessary, which seems to be rather unlikely for good-quality single crystals as those used here. Let us note for consistency that the electronic density is only reduced by approximately one order of magnitude, from $n_0 = 1.3 \times 10^{10}$ cm⁻³ down to $n_1 = 1.2 \times 10^9$ cm⁻³. So that this electronic density change is hardly caused by large mobile ionic defect concentrations. Therefore, the initial assumption about the domination of electronic over ionic conductivity $\sigma_e \gg \sigma_i$ is consistent with our findings.

The dissimilar time response observed between poling and recovering without applied electrical field in terms of the intrinsic ionic dynamics allows us to preclude alternative explanation for the measurements. One might think about slow decomposition or doping by environmental molecules as H₂O or oxygen in a surface mechanism. These kinds of processes usually involve chemical reactivity, either with the perovskite or contact materials. However, such chemical interactions usually exhibit poor reversibility. For instance, hydrated phases have been studied by first-principle methods^[42] as one of the primary degradation or decomposition paths. For solar cells structures, electrical degradation takes place on a short time scale of 2–3 days of exposure.^[43] Some authors have observed reversible responses upon drying,^[44,45] but the devices have to be exposed to dry nitrogen or high temperature for hours. Single crystals used here were always in ambient atmosphere and room temperature. If humidity was absorbed (water molecule diffusivity is much lower in mono- than in polycrystals), they should have been kept inside in contradiction to the observed reversibility in Figure S3, Supporting Information. Then the effect of extrinsic agents can be safely excluded.

Recalling now the general impedance response of Figure 2, the low-frequency feature manifested either as a linear increment (Figure 2a) or a capacitive step (Figure 2b) should be related to the dynamics of the ionic profile. The variation of the ion distribution within the time window corresponding to the measuring frequency gives rise to the reported capacitance increase because of ion accumulation C_s . Consequently, there is a modulation of the electronic doping restricted within the crystal to affected zones. The final effect is an increment in the electronic resistance caused by the coupling between ion distribution variation and carrier density. As observed in Figure 2a, the modulation effect is more visible for longer releasing times (wider distributions of mobile ions) than in the case of narrow accumulations. It is also noted that diffusion characteristics are also present in the low-frequency impedance in the form of Warburg-like responses.^[44]

In the following, we speculate about the connection between specific ionic defects and electronic doping mechanisms. Due to the presence of three elements in the ABX₃ perovskite

formulations and to the rich redox chemistry of halide-containing materials, a whole array of ionic defects (D) may be present in the crystals. The energy of defect formation has been extensively studied by theoretical calculations.^[46–48] Not only do they include the basic nine species arising from vacancies, interstitial elements, and antisites but they also include their corresponding stable charged counterparts. Examples of negatively charged defects (D^-) compatible with low formation energies include halide interstitials (X_i^-) or Pb^{2+} vacancies (V_{Pb}^{2-}). Alternatively, examples of positively charged defects (D^+) include MA^+ interstitials (MA_i^+) and Pb^{2+} interstitial (Pb_i^+) or X^- vacancies (V_X^+). Among all these defects, V_X^+ is the mobile ion believed to have the lowest activation energy for migration. While formation of these defects is accessible by theoretical means, they are very difficult to detect experimentally. As a consequence, accessible understanding of the defect density for the different defect species is always limited for given perovskite samples. Direct measurement of specific defect densities is out of the scope of this work^[49,50] and we next provide a general discussion on how the doping concentration is modified during the application and switching-off of an external bias.

A simple explanation would consist in assuming that halide vacancies V_X^+ dominate and establish the general background doping character. As V_X^+ is considered a shallow donor both for iodide and bromide perovskites,^[51,52] one can infer that n-type doping increases in zones in which the halide vacancy concentration is higher. Upon poling, accumulation of halide vacancies near the negative-biased contact is expected. As a consequence, this process forms an internal doping profile that implies that the perovskite bulk can be modeled as a sort of semiconductor homojunction with a mobile boundary between lower- and higher-doped regions in accordance with the simple structure sketched in Figure 5 of the dynamic doping process.

But obviously, the defect chemistry in hybrid perovskite compounds may be much richer. Since the application of an external voltage produces movement of charged defects and electronic carrier injection, defects can capture a hole/electron to form neutral states D^0 . Consequently, for negatively charged defects this would be $D^- + h^+ \rightarrow D^0$.^[47] However, there will be a complementary redox semi-reaction (reduction) taking place simultaneously somewhere in the device that would increase the concentration of negatively charged species. For the previous example, the complementary reduction reaction can be represented as $D^0 + e^- \rightarrow D^-$. The overall result is that there will be no change in the background doping density. If the same halogen participates in both oxidation and reduction reaction, a Frenkel type reaction will be taking place ($Br_i^- + V_{Br}^+ \rightarrow Br^0$). It has been also reported that formation of new nonradiative defects in $MAPbI_3$ is only observed in the presence of injected electrons, suggesting that redox processes play a key role.^[53]

In any case, an increase in the measured resistance as a consequence of a reduction in doping density can only be explained by formation of separated regions with different doping densities, being the least doped region mainly responsible for the resistive response. This situation is the basis of the electrical model proposed in this work that is in good agreement with previous results in spatially resolved PL measurements.^[36]

Mobile ions will follow the external electrical field induced by the external voltage and will populate the region where they can modify the doping concentration. Upon switching-off the external voltage, mobile ions (V_X^+) will move in the perovskite layer following the chemical potential generated from the highly populated region of mobile ions to the region with lower concentration of mobile ions. In the presence of an external voltage, the density of electrons and holes will be the sum of the free carriers and the background densities in each region. Alternatively, in the absence of an applied voltage, supply of h^+ / e^- to accomplish the opposite reactions will be reduced as only background doping is present in the perovskite layer. This by itself responds for the slower kinetics of the relaxation of ions after switching-off the voltage as both electrons and holes are involved in the bulk perovskite chemical reactions.

4. Conclusions

We report on the impedance analysis of a set of high-quality thick $CH_3NH_3PbBr_3$ single crystals contacted with more stable and less reacting chromium electrodes. It is shown that the high-frequency circuit elements extracted from impedance originated by the dielectric and electronic conduction properties of the sample bulk. The bias and time dependence of bulk resistance informs about the accumulation and relaxation dynamics of the moving ionic species. Our analysis extracts values for the ion diffusivity in the range of $10^{-8} \text{ cm}^2 \text{ s}^{-1}$ in good agreement with independent measurements. It is concluded that the interplay between ionic and electronic properties in perovskite materials relies upon a sort of dynamic doping effect caused by moving ions that act as dopants and locally vary the carrier density. These findings highlight the electronic-ionic coupling effect and reveals the mechanism through which such connection occurs.

5. Experimental Section

Crystal Preparation: Self-supported $CH_3NH_3PbBr_3$ single crystals were fabricated using the inverse temperature protocol in dimethylformamide (DMF), and following the growth methodology detailed in a previous work.^[29] Bare crystals have square shape with typical lateral dimensions of $5 \times 5 \text{ mm}^2$ and a thickness of 2 mm. Crystals with different thicknesses ranging from 0.6 to 1.4 mm were subsequently fabricated by using a first rough mechano-chemical polishing and by decreasing progressively the sand paper roughness. Special attention was paid to apply a pressure of less than 30 kPa on all the samples, in order to avoid any additional mechanical strains in the bulk of the crystals. In the final step, the crystals were finely polished to mirror grade quality on the (100) faces. Just after the polishing step, 100 nm thick chromium electrodes were evaporated on both faces through a mechanical shadow mask. Devices were stored in air without any encapsulation.

Impedance Measurements: Impedance spectroscopy experiments were carried out by using a PGSTAT-30 Autolab potentiostat equipped with impedance module. All the samples were measured inside a metallic box acting as Faraday cage, in dark and air conditions between 10 and 1 MHz, with a perturbation amplitude of 30 mV. Different potentials cycles were used mainly from 0 to 5 V (forward polarization bias) and from 5 to 0 V (reverse polarization bias). After each bias change, the sample was left to attain equilibrium during 5 min before starting a run. Each run lasted 13–15 min.

Supporting Information

Supporting Information is available from the Wiley Online Library or from the author.

Acknowledgements

The authors acknowledge the support from Horizon 2020 project (grant number 871336—PEROXIS). M.G.-B. acknowledges Generalitat Valenciana for a grant (number GRISOLIAP/2018/073). O.B. acknowledges Trixell for her Ph.D. grant.

Conflict of Interest

The authors declare no conflict of interest.

Keywords

dynamic doping, electronic conductivity, hybrid perovskites, ion dynamics

Received: May 8, 2020

Revised: July 7, 2020

Published online:

- [1] M. A. Green, E. D. Dunlop, J. Hohl-Ebinger, M. Yoshita, N. Kopidakis, A. W. Y. Ho-Baillie, *Prog. Photovoltaics* **2020**, *28*, 3.
- [2] W. Heiss, C. Brabec, *Nat. Photonics* **2016**, *10*, 288.
- [3] E. L. Unger, E. T. Hoke, C. D. Bailie, W. H. Nguyen, A. R. Bowring, T. Heumuller, M. G. Christoforo, M. D. McGehee, *Energy Environ. Sci.* **2014**, *7*, 3690.
- [4] J. M. Aspiroz, E. Mosconi, J. Bisquert, F. De Angelis, *Energy Environ. Sci.* **2015**, *8*, 2118.
- [5] S. Meloni, T. Moehl, W. Tress, M. Franckevičius, M. Saliba, Y. H. Lee, P. Gao, M. K. Nazeeruddin, S. M. Zakeeruddin, U. Rothlisberger, M. Graetzel, *Nat. Commun.* **2016**, *7*, 10334.
- [6] E. T. Hoke, D. J. Slotcavage, E. R. Dohner, A. R. Bowring, H. I. Karunadasa, M. D. McGehee, *Chem. Sci.* **2015**, *6*, 613.
- [7] C.-S. Jiang, M. Yang, Y. Zhou, B. To, S. U. Nanayakkara, J. M. Luther, W. Zhou, J. J. Berry, J. van de Lagemaat, N. P. Padture, K. Zhu, M. M. Al-Jassim, *Nat. Commun.* **2015**, *6*, 8397.
- [8] V. W. Bergmann, Y. Guo, H. Tanaka, I. M. Hermes, D. Li, A. Klasen, S. A. Bretschneider, E. Nakamura, R. Berger, S. A. L. Weber, *ACS Appl. Mater. Interfaces* **2016**, *8*, 19402.
- [9] M. Ahmadi, L. Collins, K. Higgins, D. Kim, E. Lukosi, S. V. Kalinin, *ACS Appl. Mater. Interfaces* **2019**, *11*, 41551.
- [10] O. Almora, C. Aranda, I. Zarazua, A. Guerrero, G. Garcia-Belmonte, *ACS Energy Lett.* **2016**, *1*, 209.
- [11] J. Wang, S. P. Senanayak, J. Liu, Y. Hu, Y. Shi, Z. Li, C. Zhang, B. Yang, L. Jiang, D. Di, A. V. Ilevlev, O. S. Ovchinnikova, T. Ding, H. Deng, L. Tang, Y. Guo, J. Wang, K. Xiao, D. Venkateshvaran, L. Jiang, D. Zhu, H. Sirringhaus, *Adv. Mater.* **2019**, *31*, 1902618.
- [12] O. Almora, I. Zarazua, E. Mas-Marza, I. Mora-Sero, J. Bisquert, G. Garcia-Belmonte, *J. Phys. Chem. Lett.* **2015**, *6*, 1645.
- [13] O. Almora, A. Guerrero, G. Garcia-Belmonte, *Appl. Phys. Lett.* **2016**, *108*, 043903.
- [14] H. Wang, A. Guerrero, A. Bou, A. M. Al-Mayouf, J. Bisquert, *Energy Environ. Sci.* **2019**, *12*, 2054.
- [15] J. Pospisil, A. Guerrero, O. Zmeskal, M. Weiter, J. J. Gallardo, J. Navas, G. Garcia-Belmonte, *Adv. Funct. Mater.* **2019**, *29*, 1900881.
- [16] J. Carrillo, A. Guerrero, S. Rahimnejad, O. Almora, I. Zarazua, E. Mas-Marza, J. Bisquert, G. Garcia-Belmonte, *Adv. Energy Mater.* **2016**, *6*, 1502246.
- [17] A. Solanki, A. Guerrero, Q. Zhang, J. Bisquert, T. C. Sum, *J. Phys. Chem. Lett.* **2020**, *11*, 463.
- [18] Y. Liu, Z. Yang, D. Cui, X. Ren, J. Sun, X. Liu, J. Zhang, Q. Wei, H. Fan, F. Yu, X. Zhang, C. Zhao, S. Liu, *Adv. Mater.* **2015**, *27*, 5176.
- [19] W. Peng, L. Wang, B. Murali, K.-T. Ho, A. Bera, N. Cho, C.-F. Kang, V. M. Burlakov, J. Pan, L. Sinatra, C. Ma, W. Xu, D. Shi, E. Alarousu, A. Goriely, J.-H. He, O. F. Mohammed, T. Wu, O. M. Bakr, *Adv. Mater.* **2016**, *28*, 3383.
- [20] M. I. Saidaminov, A. L. Abdelhady, B. Murali, E. Alarousu, V. M. Burlakov, W. Peng, I. Dursun, L. Wang, Y. He, G. Maculan, A. Goriely, T. Wu, O. F. Mohammed, O. M. Bakr, *Nat. Commun.* **2015**, *6*, 7586.
- [21] A. Kovalenko, J. Pospisil, J. Krajcovic, M. Weiter, A. Guerrero, G. Garcia-Belmonte, *Appl. Phys. Lett.* **2017**, *111*, 163504.
- [22] M. Kaltenbrunner, G. Adam, E. D. Glowacki, M. Drack, R. Schwödiauer, L. Leonat, D. H. Apaydin, H. Groiss, M. C. Scharber, M. S. White, N. S. Sariciftci, S. Bauer, *Nat. Mater.* **2015**, *14*, 1032.
- [23] L. R. Jordan, A. J. Betts, K. L. Dahm, P. A. Dearnley, G. A. Wright, *Corros. Sci.* **2005**, *47*, 1085.
- [24] A. Guerrero, J. You, C. Aranda, Y. S. Kang, G. Garcia-Belmonte, H. Zhou, J. Bisquert, Y. Yang, *ACS Nano* **2016**, *10*, 218.
- [25] S. Bai, P. Da, C. Li, Z. Wang, Z. Yuan, F. Fu, M. Kawecki, X. Liu, N. Sakai, J. T.-W. Wang, S. Huettner, S. Buecheler, M. Fahlman, F. Gao, H. J. Snaith, *Nature* **2019**, *571*, 245.
- [26] H. M. Thirimanne, K. D. G. I. Jayawardena, A. J. Parnell, R. M. I. Bandara, A. Karalasingam, S. Pani, J. E. Huerdler, D. G. Lidzey, S. F. Tedde, A. Nisbet, C. A. Mills, S. R. P. Silva, *Nat. Commun.* **2018**, *9*, 2926.
- [27] L. Basiricò, S. P. Senanayak, A. Ciavatti, M. Abdi-Jalebi, B. Fraboni, H. Sirringhaus, *Adv. Funct. Mater.* **2019**, *29*, 1902346.
- [28] S. A. L. Weber, I. M. Hermes, S.-H. Turren-Cruz, C. Gort, V. W. Bergmann, L. Gilson, A. Hagfeldt, M. Graetzel, W. Tress, R. Berger, *Energy Environ. Sci.* **2018**, *11*, 2404.
- [29] S. Amari, J.-M. Verilhac, E. Gros D'Aillon, A. Ibanez, J. Zaccaro, *Cryst. Growth Des.* **2020**, *20*, 1665.
- [30] J. T. Tisdale, E. Muckley, M. Ahmadi, T. Smith, C. Seal, E. Lukosi, I. N. Ivanov, B. Hu, *Adv. Mater. Interfaces* **2018**, *5*, 1800476.
- [31] N. Onoda-Yamamuro, T. Matsuo, H. Suga, *J. Phys. Chem. Solids* **1992**, *53*, 935.
- [32] S. Govinda, B. P. Kore, M. Bokdam, P. Mahale, A. Kumar, S. Pal, B. Bhattacharyya, J. Lahnsteiner, G. Kresse, C. Franchini, A. Pandey, D. D. Sarma, *J. Phys. Chem. Lett.* **2017**, *8*, 4113.
- [33] J. N. Wilson, J. M. Frost, S. K. Wallace, A. Walsh, *APL Mater.* **2019**, *7*, 010901.
- [34] O. Baussens, L. Maturana, S. Amari, J. Verilhac, L. Hirsch, E. Gros-Daillon, *Appl. Phys. Lett.* **2020**, *117*, 041904.
- [35] D. Shi, V. Adinolfi, R. Comin, M. Yuan, E. Alarousu, A. Buin, Y. Chen, S. Hoogland, A. Rothenberger, K. Katsiev, Y. Losovyj, X. Zhang, P. A. Dowben, O. F. Mohammed, E. H. Sargent, O. M. Bakr, *Science* **2015**, *347*, 519.
- [36] C. Li, A. Guerrero, S. Huettner, J. Bisquert, *Nat. Commun.* **2018**, *9*, 5113.
- [37] C. Eames, J. M. Frost, P. R. F. Barnes, B. C. O'Regan, A. Walsh, M. S. Islam, *Nat. Commun.* **2015**, *6*, 7497.
- [38] M. Bag, L. A. Renna, R. Y. Adhikari, S. Karak, F. Liu, P. M. Lahti, T. P. Russell, M. T. Tuominen, D. Venkataraman, *J. Am. Chem. Soc.* **2015**, *137*, 13130.

- [39] G. Richardson, S. E. J. O'Kane, R. G. Niemann, T. A. Peltola, J. M. Foster, P. J. Cameron, A. B. Walker, *Energy Environ. Sci.* **2016**, 9, 1476.
- [40] T.-Y. Yang, G. Gregori, N. Pellet, M. Grätzel, J. Maier, *Angew. Chem., Int. Ed.* **2015**, 54, 7905.
- [41] W. Peng, C. Aranda, O. M. Bakr, G. Garcia-Belmonte, J. Bisquert, A. Guerrero, *ACS Energy Lett.* **2018**, 3, 1477.
- [42] Y.-H. Kye, C.-J. Yu, U.-G. Jong, Y. Chen, A. Walsh, *J. Phys. Chem. Lett.* **2018**, 9, 2196.
- [43] A. Marronnier, H. Lee, H. Lee, M. Kim, C. Eypert, J.-P. Gaston, G. Roma, D. Tondelier, B. Geffroy, Y. Bonnassieux, *Sol. Energy Mater. Sol. Cells* **2018**, 178, 179.
- [44] A. M. A. Leguy, Y. Hu, M. Campoy-Quiles, M. I. Alonso, O. J. Weber, P. Azarhoosh, M. van Schilfgaarde, M. T. Weller, T. Bein, J. Nelson, P. Docampo, P. R. F. Barnes, *Chem. Mater.* **2015**, 27, 3397.
- [45] A. García-Fernández, Z. Moradi, J. M. Bermúdez-García, M. Sánchez-Andújar, V. A. Gimeno, S. Castro-García, M. A. Señarís-Rodríguez, E. Mas-Marzá, G. Garcia-Belmonte, F. Fabregat-Santiago, *J. Phys. Chem. C* **2019**, 123, 2011.
- [46] D. Meggiolaro, E. Mosconi, F. De Angelis, *ACS Energy Lett.* **2018**, 3, 447.
- [47] L. D. Whalley, R. Crespo-Otero, A. Walsh, *ACS Energy Lett.* **2017**, 2, 2713.
- [48] S. G. Motti, D. Meggiolaro, A. J. Barker, E. Mosconi, C. A. R. Perini, J. M. Ball, M. Gandini, M. Kim, F. De Angelis, A. Petrozza, *Nat. Photonics* **2019**, 13, 532.
- [49] D. W. deQuilettes, K. Frohna, D. Emin, T. Kirchartz, V. Bulovic, D. S. Ginger, S. D. Stranks, *Chem. Rev.* **2019**, 119, 11007.
- [50] L. Bertoluzzi, C. C. Boyd, N. Rolston, J. Xu, R. Prasanna, B. C. O'Regan, M. D. McGehee, *Joule* **2020**, 4, 109.
- [51] W.-J. Yin, T. Shi, Y. Yan, *Appl. Phys. Lett.* **2014**, 104, 063903.
- [52] S. G. Motti, D. Meggiolaro, S. Martani, R. Sorrentino, A. J. Barker, F. De Angelis, A. Petrozza, *Adv. Mater.* **2019**, 31, 1901183.
- [53] S. T. Birkhold, J. T. Pecht, H. Liu, R. Giridharagopal, G. E. Eperon, L. Schmidt-Mende, X. Li, D. S. Ginger, *ACS Energy Lett.* **2018**, 3, 1279.